



# One-dimensional phase-field model for binary alloys

D.I. Popov<sup>1</sup>, L.L. Regel\*, W.R. Wilcox

*Int. Ctr. Gravity Mat. Sci. & Appl., Clarkson University, Box 5814, Potsdam, NY 13699-5814, USA*

Received 24 May 1999; accepted 5 January 2000

Communicated by R.S. Feigelson

## Abstract

A phase-field model was developed that gives an accurate solution for the equilibrium partition of single-phase alloy. It also gives the correct volume fractions and compositions of a two-phase solid binary alloy at equilibrium. Application to oscillatory solidification produced solute striations in the resulting single-phase solid. This one-dimensional modeling was carried out as a test for our two-dimensional model of unsteady lamellar eutectic solidification. © 2000 Elsevier Science B.V. All rights reserved.

PACS: 64.70.D; 81.10.F; 81.30.F

Keywords: Phase-field method; Segregation; Impurity striations; Eutectic solidification; Oscillatory solidification

## 1. Formulation of the phase-field model for a two-phase, two-component system

To simulate unsteady freezing, we developed numerically a phase-field model of solidification, e.g., Ref. [1]. The advantage of the phase-field formulation is that no computational distinction is made between solid, liquid, and interface. This allows the whole domain to be treated in the same way numerically. The interface is not tracked, but is given implicitly by a scalar function of space and time, called the phase field. The phase-field parameter  $\phi$  is governed by a partial differential equation that guarantees that (in the limit of an infinitely thin interface region) the appropriate boundary conditions at the crystal/melt interface are satisfied.

The evolution equation for  $\phi$  in the Ginzburg–Landau approach is a Langevin equation neglecting a Gaussian white noise source, which can be written as [2]

$$\frac{\partial \phi}{\partial t} = -\frac{1}{\tau} \left( \frac{\delta F(\phi)}{\delta \phi} \right). \quad (1)$$

Here  $\tau$  is the relaxation coefficient, which sets the microscopic time scale for order-parameter relaxation and is assumed to be independent of  $\phi$ . The free energy  $F$  is chosen to have two minima, corresponding to the two phases at equilibrium. The free energy consists of the Cahn–Hilliard [3] term including the double-well and gradient free energy, and a non-equilibrium driving term, which is the phase-dependent bulk free energy [1]:

$$f_L(c, T) = [cZ_1(T) + (1 - c)Z_2(T)] + \frac{RT}{v_m} [c \ln c + (1 - c) \ln(1 - c)], \quad (2)$$

\* Corresponding author. Fax: + 1-315-268-3833.

E-mail address: regel@clarkson.edu (L.L. Regel).

<sup>1</sup> Current address: Department of Physics, State University of New York at Brockport, Brockport, NY 14420, USA.

where  $c$  is the mole fraction of component-1 in the liquid phase, and the functions  $Z_1(T)$  and  $Z_2(T)$  are

$$Z_1(T) = C_{v1}(T - T_0) - TC_{v1} \ln\left(\frac{T}{T_0}\right),$$

$$Z_2(T) = C_{v2}(T - T_0) - TC_{v2} \ln\left(\frac{T}{T_0}\right). \quad (3)$$

Here  $C_{vi}$  is the specific heat of pure component  $i$  ( $i = 1, 2$ ) and  $T_0$  is an arbitrary reference temperature. We assume that the specific heat is equal for both components, i.e.  $C_{v1} = C_{v2}$ , so that  $Z(T) = Z_1(T) = Z_2(T)$ . The first term in brackets in Eq. (2) is associated with the energy densities due to the individual Helmholtz free energy densities of the pure components. The second is the free energy associated with the mixing of two components to form an ideal solution, where  $R$  is the ideal gas constant and  $v_m$  is the molar volume (here assumed to be constant and the same for both components).

The free energy for the solid phase can be written in a form similar to Eq. (2)

$$f_S(c, T) = [cZ_1(T) + (1 - c)Z_2(T)] + \frac{RT}{v_m} [c \ln c + (1 - c) \ln(1 - c)] - [cf_1(T) + (1 - c)f_2(T)], \quad (4)$$

where the last term in Eq. (4) is associated with the excess free energy of the phase transformation. The functions  $f_1$  and  $f_2$  correspond to the pure components, and have the form

$$f_1(T) = \Delta H_1 \left(1 - \frac{T}{T_1}\right),$$

$$f_2(T) = \Delta H_2 \left(1 - \frac{T}{T_2}\right), \quad (5)$$

where  $\Delta H_i$  is the enthalpy of fusion of pure component  $i$  ( $i = 1, 2$ ), and  $T_i$  is the melting point of that component.

### 1.1. Phase field

The phase-field formulation for alloy solidification employs the free energy, which is also

phase-dependent. As in Ref. [1], the free energy is written as

$$f(\phi, c, T) = h(\phi)f_L(c, T) + (1 - h(\phi))f_S(c, T), \quad (6)$$

where  $h(\phi)$  is a polynomial function of the phase-field parameter  $\phi$ . In the present model it has the form

$$h(\phi) = \frac{3}{4}\phi - \frac{1}{4}\phi^3 + \frac{1}{2} \quad (7)$$

with the following properties:

$$h(-1) = 0, \quad h(0) = \frac{1}{2}, \quad h(1) = 1,$$

$$\frac{\partial h(\phi)}{\partial \phi} = \frac{3}{4}(1 - \phi^2),$$

$$\left. \frac{\partial h(\phi)}{\partial \phi} \right|_{\phi=-1} = 0, \quad \left. \frac{\partial h(\phi)}{\partial \phi} \right|_{\phi=0} = \frac{3}{4}, \quad \left. \frac{\partial h(\phi)}{\partial \phi} \right|_{\phi=1} = 0. \quad (8)$$

Substituting  $f_S(c, T)$  and  $f_L(c, T)$  into Eq. (6), the free energy in the phase-field formulation is

$$f(\phi, c, T) = Z(T) + \frac{RT}{v_m} [c \ln c + (1 - c) \ln(1 - c)] - (1 - h(\phi))[cf_1(T) + (1 - c)f_2(T)]. \quad (9)$$

The explicit form of Eq. (1) after substitution into Eq. (9) takes the form

$$\frac{\partial \phi}{\partial t} = \frac{1}{\tilde{\tau}} \left\{ \varepsilon^2 \nabla^2 \phi + W(\phi - \phi^3) - \frac{\partial h(\phi)}{\partial \phi} \left( \Delta H_1 \left(1 - \frac{T}{T_1}\right) c + \Delta H_2 \left(1 - \frac{T}{T_2}\right) (1 - c) \right) \right\}, \quad (10)$$

where  $\tilde{\tau} = \tau T$ .

We assume, for simplicity, that the interface properties, i.e. the interfacial free energy  $\sigma$  and the effective width  $\delta$  of the interface, are independent of composition. This means that the phase-field parameters  $\varepsilon$ ,  $W$ , and  $\tau$  are also independent of composition. Using the approach developed in Refs. [3,4], we found the relationship between the phase-field parameters  $\varepsilon$ ,  $W$ ,  $\tau$  and the physical parameters; interfacial energy  $\sigma$ , interface thickness  $\delta$ , and

kinetic coefficient (interface mobility)  $\beta$

$$\varepsilon = \frac{\sqrt{3\sigma\delta}}{2\sqrt{2}}, \quad W = \frac{3\sigma}{\delta}, \quad \tau = \frac{3\delta\Delta\bar{S}}{8\beta} \quad (11)$$

and  $\Delta\bar{S} = (\Delta S_1[(T_1 - \bar{T})/(T_m - \bar{T})] + \Delta S_2[(T_2 - \bar{T})/(T_m - \bar{T})](1 - \bar{c}))$ . The free energy difference between the phases is the excess free energy of the phase transformation, directly related to the latent heat given by the last term in Eq. (9).

1.2. Composition field

The evolution of the composition field can be described by [1]

$$\frac{\partial c}{\partial t} = -\nabla \cdot \left\{ \frac{D(\phi)v_m}{R} c(1-c) \nabla \left[ \frac{\Delta\mu(\phi, c, T)}{T} \right] \right\}, \quad (12)$$

where  $\Delta\mu$  is the difference between the chemical potentials of the two components, and  $v_m$  is the average molar volume of components 1 and 2. The mass diffusivity  $D(\phi)$  is phase-dependent. A realistic case is a very large difference between the solid and liquid diffusivities [5]. The following variation was used in the present calculations

$$D(\phi) = h(\phi)D_{\text{liquid}} + (1 - h(\phi))D_{\text{solid}}. \quad (13)$$

The chemical potentials of the two components also depend on the order parameter  $\phi$ . The chemical potential difference is found from the bulk free energy to be

$$\Delta\mu = \frac{RT}{v_m} \ln\left(\frac{c}{1-c}\right) - (1 - h(\phi)) \left\{ \Delta H_1 \left(1 - \frac{T}{T_1}\right) - \Delta H_2 \left(1 - \frac{T}{T_2}\right) \right\}. \quad (14)$$

After substitution of Eq. (14) into Eq. (12), the r.h.s. of Eq. (12) can be divided into three parts in order to solve Eq. (12):

$$\begin{aligned} \frac{\partial c}{\partial t} = & D(\phi)\Xi_1(\phi, \nabla\phi, c, \nabla c, T) \\ & + D(\phi)\Xi_2(\phi, \nabla\phi, c, \nabla c, T, \nabla T) \\ & + (\partial D(\phi)/\partial\phi)\Xi_3(\phi, \nabla\phi, c, \nabla c, T, \nabla T) \end{aligned} \quad (15)$$

where  $\Xi_1$ ,  $\Xi_2$ , and  $\Xi_3$  are the following

$$\begin{aligned} \Xi_1 = & \nabla^2 c + \left\{ \frac{v_m}{RT} \frac{\partial h(\phi)}{\partial\phi} (f_1 - f_2)(1 - 2c) \right\} \nabla c \nabla\phi \\ & + \left\{ \frac{v_m}{RT} (f_1 - f_2)c(1 - c) \right\} \\ & \times \left( \frac{\partial h(\phi)}{\partial\phi} \nabla^2\phi + \frac{\partial^2 h(\phi)}{\partial\phi^2} (\nabla\phi)^2 \right), \end{aligned} \quad (16a)$$

$$\begin{aligned} \Xi_2 = & \left\{ \frac{2v_m}{RT^2} \frac{\partial h(\phi)}{\partial\phi} (-\Delta H_1 - \Delta H_2)c(1 - c) \right\} \nabla\phi \nabla T \\ & + \left\{ \frac{v_m}{RT^2} (-h(\phi)(\Delta H_1 - \Delta H_2)(1 - 2c)) \right\} \nabla c \nabla T \\ & + \left\{ \frac{v_m}{RT^2} (-h(\phi)(\Delta H_1 - \Delta H_2)c(1 - c)) \right\} \\ & \times \left( \nabla^2 T - \frac{2}{T} (\nabla T)^2 \right), \end{aligned} \quad (16b)$$

$$\begin{aligned} \Xi_3 = & \nabla c \nabla\phi + \left\{ \frac{v_m}{RT} \frac{\partial h(\phi)}{\partial\phi} (f_1 - f_2)c(1 - c) \right\} (\nabla\phi)^2 \\ & + \left\{ \frac{v_m}{RT} (-h(\phi)(\Delta H_1 - \Delta H_2)c(1 - c)) \right\} \nabla\phi \nabla T. \end{aligned} \quad (16c)$$

The reasons to divide Eq. (15) into three parts (16a)–(16c) in the solution procedure are

- (a) With a finite domain and  $T$  constant, the solution of Eq. (12) should evolve to equilibrium between the bulk solid and liquid phases, as given by the phase diagram. The segregation coefficient  $k$  equals  $c_s/c_L$  where  $c_s$  and  $c_L$  are for  $\phi = -1$  and  $\phi = 1$ , respectively. We tested the convergence of our model by assuming  $D_{\text{Liquid}} = D_{\text{Solid}}$ . Since the temperature is constant throughout the domain,  $\Xi_2$  is zero. The condition  $D_{\text{Liquid}} = D_{\text{Solid}}$  makes  $\Xi_3$  zero.
- (b) After equilibrium was reached, the temperature at the ends of the computational domain were changed. We then accounted for  $\nabla T \neq 0$  and  $D_{\text{Liquid}} \neq D_{\text{Solid}}$ . New terms containing  $\partial D(\phi)/\partial\phi$  and  $\nabla T$  are necessary, and  $\Xi_2$  and  $\Xi_3$  are not equal to zero.

### 1.3. Temperature field

The temperature field in the absence of convection is governed by

$$\frac{\partial H}{\partial t} = \nabla \{K(\phi, c, T) \nabla T\}, \quad (17)$$

where  $K(\phi, c, T)$  is the thermal conductivity. In general, its value depends on phase, composition and temperature. For simplicity here, we assume that the thermal conductivity is constant and the same for both liquid and solid, i.e.  $K(\phi) = K$ . The enthalpy is written as

$$H(\phi, c, T) = C_v(T - T_0) - (1 - h(\phi)) \times [c\Delta H_1 + (1 - c)\Delta H_2]. \quad (18)$$

Carrying out partial differentiation, Eq. (17) becomes

$$\frac{\partial T}{\partial t} = \alpha \nabla^2 T - \frac{\partial h(\phi)}{\partial \phi} \frac{1}{C_v} \{ \Delta H_1 c + \Delta H_2 (1 - c) \} \frac{\partial \phi}{\partial t} - \frac{1}{C_v} \{ -(1 - h(\phi))(\Delta H_1 - \Delta H_2) \} \frac{\partial c}{\partial t}, \quad (19)$$

where  $\alpha = \alpha_s = \alpha_L$  is the thermal diffusivity.

### 1.4. Equilibrium phase diagram for two-component single-phase alloy

For the following test calculations, we assumed that components 1 and 2 are completely soluble in each other. The phase diagram shown in Fig. 1 was created using the equilibrium liquidus  $c_L$  and solidus  $c_S$  compositions, and thermodynamic properties from Table 1. The procedure and equations used are given in the appendix.

## 2. Results of numerical simulations

### 2.1. Single-phase alloy solidification: implementation of the finite difference method

We applied this phase-field model to one-dimensional, single-solid-phase, two-component alloy solidification in order to obtain the conditions for accurate numerical solution of the governing equa-

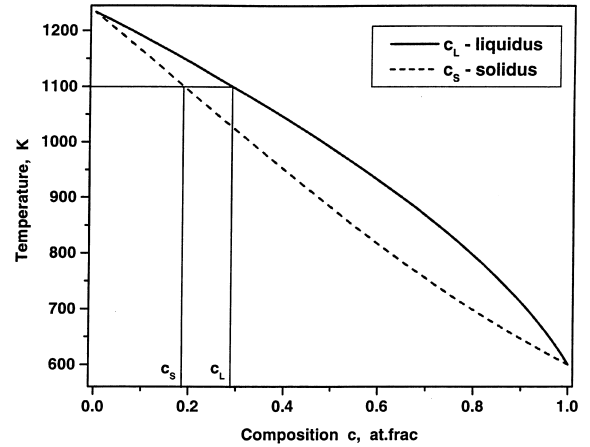


Fig. 1. Phase diagram for a single-phase model alloy. Equilibrium solid and liquid compositions are shown at 1100 K. The equilibrium liquidus  $c_L$  and solidus  $c_S$  compositions were found at several temperatures (Tables 2 and 3) by solving Eq. (A.4) using the procedure given in the appendix.

Table 1  
Thermodynamic properties of model alloy

$T_1$ (K)	$T_2$ (K)	$\Delta H_1$ (J cm <sup>-3</sup> )	$\Delta H_2$ (J cm <sup>-3</sup> )	$v_m$ (cm <sup>3</sup> mol <sup>-1</sup> )
600.0	1234.0	477.0	1130.0	10

tions (10), (15) and (19). We chose initial values of the liquid and solid compositions that do not coincide with equilibrium at the given temperature. This system should evolve to a state with the values of liquid and solid compositions corresponding to the phase diagram given in Fig. 1. For this purpose, we implemented two finite difference schemes, discretizing the system of Eqs. (10) and (15) with constant temperature and  $D(\phi)$  constant. Two schemes were chosen to show the accuracy of the results for each particular discretization scheme. Neumann boundary conditions were imposed at the boundaries for the phase-field and mass transport equations. Dirichlet boundary conditions were implemented for heat transport. An explicit Euler scheme was used for time integration. First, the simplest form of the finite-difference approximation to the governing equations was chosen, e.g. first-order central differences. The calculations were

carried out for several values of temperature, with zero enthalpy of mixing. Some of these temperatures were in the central part of the phase diagram (Fig. 1), and two ( $T = 610$  K and  $T = 1230$  K) were very close to the melting points of the pure components ( $T_1 = 600$  K,  $T_2 = 1234$  K). The results are summarized in Table 2. The differences between calculated and actual equilibrium compositions and segregation coefficient were relatively large, especially near the ends of the phase diagram.

In order to improve the accuracy of the numerical results, a second-order central difference scheme was implemented. The results are summarized in Table 3. The accuracy of the calculations was greatly improved, especially for temperatures close to the melting points of the pure components. We used 300 grid points in the calculations. A further increase in the density of grid points seemed to be unnecessary (see Table 4).

Table 2  
First-order central difference results for the model alloy with the properties given in Table 1

$T$ (K)	$c_S$ exact	$c_L$ exact	$c_S$ calcul.	$c_L$ calcul.	$\delta c_S$ error (%)	$\delta c_L$ error (%)	$k$ exact	$k$ calcul.	$\delta k$ error (%)
610	0.977	0.993	0.907	0.968	-7.24	-2.50	0.984	0.937	-4.85
650	0.892	0.960	0.835	0.935	-6.36	-2.57	0.929	0.893	-3.89
800	0.625	0.794	0.601	0.777	-3.78	-2.12	0.787	0.774	-1.69
1000	0.328	0.481	0.335	0.489	2.14	1.67	0.682	0.685	0.47
1100	0.187	0.289	0.203	0.311	8.43	7.29	0.648	0.654	1.07
1150	0.118	0.186	0.137	0.214	16.84	15.29	0.633	0.642	1.34
1200	$0.477 \times 10^{-1}$	$0.770 \times 10^{-1}$	$0.746 \times 10^{-1}$	0.119	56.42	54.16	0.620	0.629	1.37
1230	$0.560 \times 10^{-2}$	$0.920 \times 10^{-2}$	$0.153 \times 10^{-1}$	$0.246 \times 10^{-1}$	173.21	167.39	0.613	0.624	1.83

Table 3  
Second-order central difference results for the model alloy with the properties given in Table 1

$T$ (K)	$c_S$ exact	$c_L$ exact	$c_S$ calcul.	$c_L$ calcul.	$\delta c_S$ error (%)	$\delta c_L$ error (%)	$k$ exact	$k$ calcul.	$\delta k$ error (%)
610	0.977	0.993	0.966	0.989	-1.19	-0.38	0.984	0.977	-0.80
650	0.892	0.960	0.889	0.959	-0.27	-0.09	0.929	0.928	-0.17
800	0.625	0.794	0.624	0.793	-0.14	-0.08	0.787	0.787	-0.06
1000	0.328	0.481	0.328	0.481	0.03	0.02	0.682	0.682	0.02
1100	0.187	0.289	0.188	0.290	0.27	0.28	0.648	0.648	0
1150	0.118	0.186	0.118	0.187	0.68	0.59	0.633	0.634	0.08
1200	$0.477 \times 10^{-1}$	$0.770 \times 10^{-1}$	$0.487 \times 10^{-1}$	$0.789 \times 10^{-1}$	2.10	2.47	0.620	0.620	0.05
1230	$0.56 \times 10^{-2}$	$0.92 \times 10^{-2}$	$0.586 \times 10^{-2}$	$0.956 \times 10^{-2}$	4.64	3.91	0.613	0.613	0.02

Table 4  
Results for different number of grid points ( $T = 1000$  K) using second-order central difference

Number of points	Number of points on the interval $\phi = [-0.99; 0.99]$	$c_S$ calcul.	$c_L$ calcul.	$\delta c_S$ error (%)	$\delta c_L$ error (%)	$k$ calcul.	$\delta k$ error (%)
300	35	0.328	0.481	0.03	0.02	0.682	0.02
200	24	0.329	0.482	0.34	0.29	0.683	0.04
100	12	0.342	0.497	4.24	3.37	0.688	0.84

The evolution from the initial condition to equilibrium is shown in Fig. 2. The length of the computational domain was nondimensionalized with 1 corresponding to  $5 \times 10^{-2}$  cm. At the interface, the solution evolved rapidly, approaching the correct segregation coefficient and equilibrium compositions. Far from the interface, the composition changed slowly. The rate of convergence to equilibrium was governed by the diffusion coefficient. Here, we were not interested in the dynamics of the relaxation, but rather in the converged values for the bulk liquid and solid compositions.

## 2.2. Solidification in a temperature gradient; solute rejection at the interface

The initial condition for our simulation of single-phase alloy solidification in an applied temperature gradient was the equilibrium solution obtained in Section 2.1. The temperatures at the ends of the computational domain were suddenly changed to 1103 K for the hot zone and 1093 K for the cold zone. The diffusion coefficient was chosen to be phase-dependent according to Eq. (13). In the

bulk liquid phase  $D_L = 10^{-5}$  cm<sup>2</sup>/s, and in the bulk solid phase  $D_S = 10^{-7}$  cm<sup>2</sup>/s.

Fig. 3 shows the evolution in time of the phase-field parameter and temperature in the vicinity of the freezing interface. For a stationary computational domain length of  $5 \times 10^{-2}$  cm, the average temperature gradient across the interface was 200 K/cm. The temperature field evolved until a constant temperature gradient was reached. Chemical equilibrium across the interface was not preserved, and the interface moved parallel to the temperature gradient. The difference between the slopes of the temperature profiles in the bulk solid and the bulk liquid phases is related to the latent

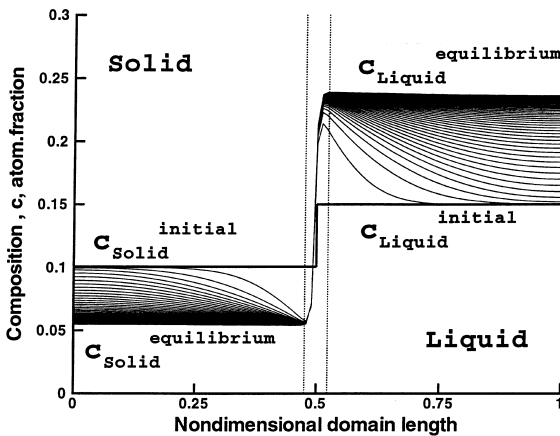


Fig. 2. The evolution of the composition field from an initial condition to equilibrium for a single phase alloy. The solution was obtained by solving a one-dimensional phase-field model for a binary alloy. The solution evolves rapidly from the initial step function at the interface, approaching the correct partition and equilibrium composition. Far from the interface the composition evolves rather slowly. The rate of convergence to equilibrium is governed by the value of the diffusion coefficient  $D$ . The domain size is  $5 \times 10^{-2}$  cm.

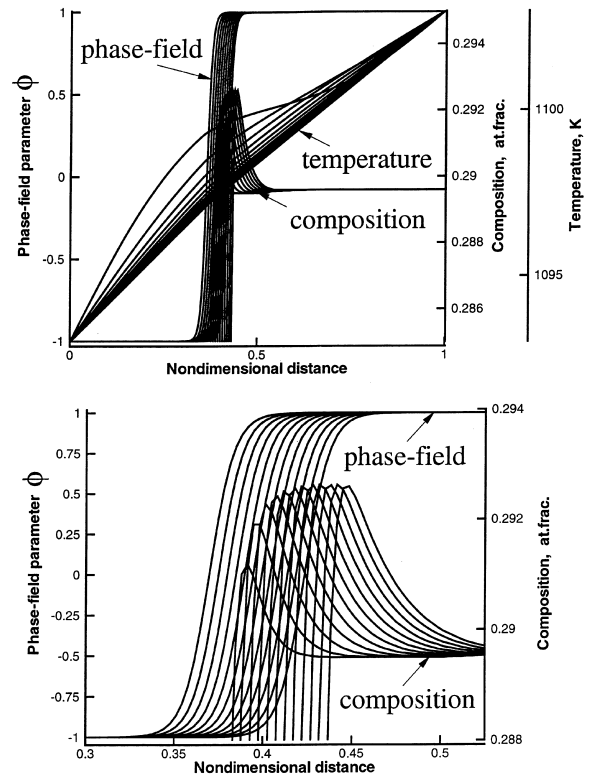


Fig. 3. (a) The evolution of the phase-field parameter  $\phi$ , composition  $c$  and temperature  $T$  after non-equilibrium temperature boundary conditions (1103 K for the hot zone and 1093 K for the cold zone) were imposed suddenly at the ends of the computational domain. The length of the domain is  $5 \times 10^{-2}$  cm, and the average temperature gradient fixed across the interface is 200 K/cm. (b) A close-up of the solute and phase field profiles near the freezing interface. The different curves represent different times. The profiles move in time from left to right.

heat release at the interface and the advancing rate of the interphase boundary. After the transient subsided, the steady state temperature profile had a constant gradient throughout the solid and the liquid.

Equilibrium composition partitioning at the interface cannot be satisfied as the interface moves in the temperature field. In the phase-field model, a high gradient of the phase-field parameter  $\phi$  in the interphase region is balanced by a chemical gradient across the interface created by an entropy jump between the bulk liquid and solid phases. The composition profile is a steep-gradient function across the interphase boundary. Closer to the bulk liquid phase where the gradient of the phase-field parameter is not high, the partitioning is not effective, and an increase in composition by partitioning is balanced by diffusion of solute away from the interface. Since the diffusion coefficient is much lower than the thermal diffusivity, reaching a steady-state distribution of composition requires much more time than does a steady-state temperature distribution. The composition profile in the melt is an exponentially decaying function with increasing distance from the interface, as in the classical sharp interface model at steady state [6].

When the temperature profile had nearly evolved into a constant gradient, we started decreasing the temperature at the hot and cold ends of the interval at equal rates. After some time, the transient was eliminated, and the maximum of the solute composition on the liquid side of the interface reached a constant value. We were more interested in qualitative behavior than in the accuracy of the numerical solution. Since in the phase-field method the composition profile across the interphase boundary is a smooth function of the spatial variable, the numerically calculated composition profile never coincides with that described by the sharp interface model. The value of the composition at the maximum on the liquid side of the interphase boundary depends on the effective boundary width  $\delta$ . Analytically, it was shown in Ref. [7] that for  $\delta \rightarrow 0$  the maximum composition approaches that from the classical sharp interface model. Numerically, to achieve as accurate results as possible, one should use a large number of computational points in the interphase region.

### 2.3. Oscillatory single-phase solidification

Our purpose was not to obtain a numerical solution coinciding with the classical solution for one-dimensional alloy solidification. Rather we pursued some issues of unsteady solidification. Freezing rate oscillations lead to periodic impurity striations in the crystal. The amplitude of these growth striations decreases when the temperature fluctuations occur rapidly. This phenomenon is attributed to a delay in the response of the rate of the interphase boundary advancement to rapid temperature fluctuations.

We applied an oscillating temperature to the hot end of the computational interval. The response of the composition field in the liquid is shown in Fig. 4(a). The lines are the composition profiles at equal time intervals. The single-period average of the maximum concentration  $c_{\max}$  increases along with the difference  $c_{\max} - c_{\min}$  as the interface advances. This happens because the freezing interface approaches the point where the oscillating temperature boundary condition is applied. Fig. 4(b) shows the resulting solute striations in the growing solid.

### 2.4. Volume fraction adjustment

As the first step in an investigation of oscillatory eutectic solidification, we developed a one-dimensional model for volume fraction adjustment of a eutectic. This model yields the correct result, with constant composition and constant volume fraction of each phase corresponding to equilibrium. If the initial condition is set different from steady state, the system evolves to adjust the compositions and volume fractions to the correct steady state values. If kinetic effects are negligible, those values of compositions and volume fractions can be found from the equilibrium phase diagram.

The model includes a phase-field parameter  $\psi$  that differs between the two solid phases. The calculations were carried out at constant temperature for three different temperatures ( $T = 750, 950$  and  $1150$  K). The initial condition was equal volume fractions of  $\alpha$ - and  $\beta$ -phases, and a constant composition of 0.8 atom fraction throughout the computational domain. The change in composition

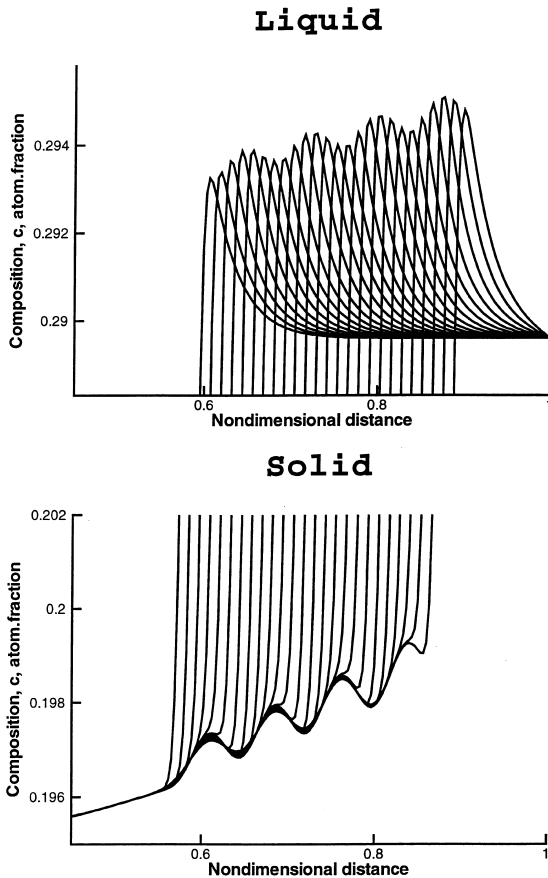


Fig. 4. Single-phase alloy solidification in an oscillatory temperature field. The domain length is  $5 \times 10^{-2}$  cm. (a) The response of the composition field in the liquid to an oscillating temperature at the hot end of the computational domain. The curves represent the composition profile at equal time steps. (b) Solute oscillations in the growing solid as a response to the composition oscillations in the liquid. In the bulk liquid phase  $D_L = 10^{-5}$  cm<sup>2</sup>/s, and in the bulk solid phase  $D_S = 10^{-7}$  cm<sup>2</sup>/s. In the interphase region, the diffusion coefficient varies according to Eq. (13).

takes place at the solid/solid boundary, which is defined by the steep gradient in the phase-field parameter  $\psi$ . Figs. 5(a)–(c) show the convergence of the solution to equilibrium, with well-defined terminal solid compositions of  $\alpha$  and  $\beta$ , and a volume fraction of these such that the solute is conserved. The composition profile had become close to that for equilibrium when the computation was stopped.

Another numerical simulation gave insight into the dynamics of the volume fraction adjustment

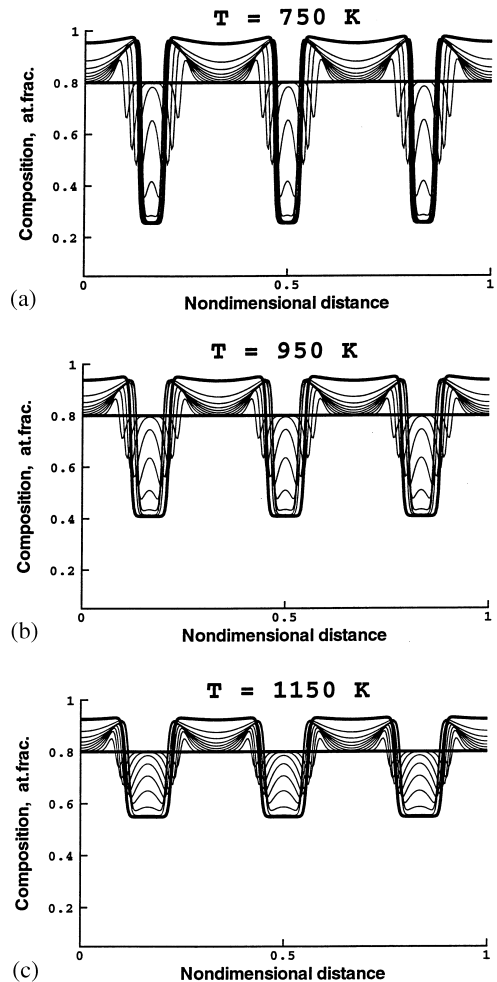


Fig. 5. Evolution to equilibrium for well-defined terminal solid compositions of  $\alpha$  and  $\beta$ , and a volume fraction such that solute is conserved: (a)  $T = 750$  K, (b)  $T = 950$  K, (c)  $T = 1150$  K. The initial conditions are equal volume fractions of  $\alpha$  and  $\beta$ , and constant composition throughout the computational domain of 0.8 atom fraction (horizontal thick line). The composition profile was close to equilibrium (another thick line) when the computation was stopped. The domain size is  $5 \times 10^{-2}$  cm.

mechanism with an oscillation of temperature. Since this model is one dimensional, the temperature is constant throughout the computational domain at every time, i.e. the temperature is a function of time only. An amplitude of 50 K was applied when the equilibrium composition and phase-field profile had been obtained for  $T = 950$  K (Fig. 5(b)). Fig. 6 shows a close-up of the composition profile

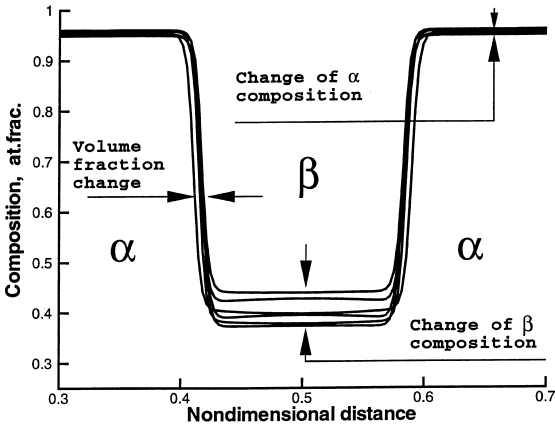


Fig. 6. An oscillating temperature in a one-dimensional two-solid phase model makes the volume fraction and the terminal solid compositions oscillate within the bounds shown by the arrows. Different curves represent the composition profile at different times. The amplitude of temperature oscillations is 50 K.

for two  $\alpha$  lamellae, one  $\beta$  and two interphase boundaries. The curves represent the composition profile at different times. Note that the composition of the phase with the larger volume fraction ( $\alpha$ ) changes less than the other ( $\beta$ ). The volume fraction does not change much even for high amplitude temperature oscillations. This model provides a simple view of oscillatory eutectic solidification [8]. However, as shown in Ref. [8], the volume fraction is not sensitive even for high amplitudes of temperature oscillations. However, accounting for the interface curvature, as in the two-dimensional model in Ref. [8], makes the interface more sensitive to temperature oscillations. Moreover, on a length scale larger than  $\lambda$ , an interface instability can be developed, the interface becomes modulated, and volume fraction adjusts since the local growth direction is changed. This inherently one-dimensional model is not suitable for modeling interface instabilities, but the result obtained in Ref. [8] for a planar interface resembles that described here.

### 3. Conclusions

The present phase-field model yielded an equilibrium solution coinciding with that from the phase

diagram. This result was independent of the width of the interphase boundary, but very sensitive to the number of computational points in the domain. For higher accuracy, the number of computational points and the CPU time would have to be increased.

The non-isothermal phase-field model included solute partition and latent heat release at the freezing interface. Solute striations resulted from an oscillatory freezing rate caused by temperature oscillations.

The phase-field approach correctly describes mass conservation, the equilibrium composition and volume fractions in a one-dimensional, two-solid-phase model. The volume fraction of the two phases did not change much even for high amplitude temperature oscillations.

### Acknowledgements

The research was supported by NASA grant NAG8-1266. We are grateful to Barbara Facemire for arranging supercomputer time at NASA Marshall Space Flight Center, and to Prof. Gunduz Caginalp for valuable discussions.

### Appendix

To find the equilibrium solid and liquid compositions in a two-component two-phase system, we used the criterion for chemical potentials [9]:

$$\Delta\mu = \mu_1^S - \mu_2^S = \mu_1^L - \mu_2^L \Rightarrow \left. \frac{\partial f_S}{\partial c} \right|_{c_S} = \left. \frac{\partial f_L}{\partial c} \right|_{c_L}. \quad (\text{A.1})$$

That is, the difference in chemical potentials between the two components in the solid phase is the same as that in the liquid phase. Geometrically this means that the two curves corresponding to the free energies of the solid and liquid phases versus composition must have the same tangent at the equilibrium composition:

$$\mu_2^S = \mu_2^L \Rightarrow f_S - c_S \left. \frac{\partial f_S}{\partial c} \right|_{c_S} = f_L - c_L \left. \frac{\partial f_L}{\partial c} \right|_{c_L}. \quad (\text{A.2})$$

These two equations are both necessary and sufficient for chemical equilibrium. Using the explicit expressions for  $f_S$  and  $f_L$ , the system (A.1), (A.2) can be written in a more convenient form as

$$\begin{cases} \ln \frac{c_L}{c_S} = -\frac{f_1 v_m}{RT} + \frac{\Omega_S v_m}{RT} (1 - c_S)^2 - \frac{\Omega_L v_m}{RT} (1 - c_L)^2, \\ \ln \frac{1 - c_L}{1 - c_S} = -\frac{f_2 v_m}{RT} + \frac{\Omega_S v_m}{RT} c_S^2 - \frac{\Omega_L v_m}{RT} c_L^2, \end{cases} \quad (\text{A.3})$$

where  $\Omega_S$  and  $\Omega_L$  are the excess enthalpies of mixing of the solid and the liquid, and  $v_m$  is the average molar volume of the alloy. This system can be solved numerically using Newton's method (by Maple, for example). For  $\Omega_S = \Omega_L = 0$ , Eq. (A.3) can be solved analytically to yield

$$\begin{aligned} c_L &= \frac{-1 + \exp(f_2 v_m / RT)}{\exp(f_1 v_m / RT) - \exp(f_2 v_m / RT)}, \\ c_S &= \frac{(-1 + \exp(f_2 v_m / RT)) \exp(f_1 v_m / RT)}{\exp(f_1 v_m / RT) - \exp(f_2 v_m / RT)}. \end{aligned} \quad (\text{A.4})$$

The calculated values for  $c_S$  and  $c_L$  appearing in Tables 2–4 are the values obtained from the analytical solution of Eq. (A.4).

## References

- [1] G. Caginalp, J. Jones, *Ann. Phys.* 237 (1995) 66.
- [2] J.S. Langer, Models of pattern formation in first-order phase transitions, in: G. Grinstein, G. Mazenko (Eds.), *Directions in Condensed Matter Physics*, Vol. 1, World Scientific Publ. Co., Singapore, 1986, pp. 165–186.
- [3] J.W. Cahn, J.E. Hilliard, *J. Chem. Phys.* 28 (1958) 258.
- [4] S.M. Allen, J.W. Cahn, *Acta Metall.* 27 (1979) 1085.
- [5] M. Conti, *Phys. Rev. E* 55 (1997) 765.
- [6] W.A. Tiller, K.A. Jackson, J.W. Rutter, B. Chalmers, *Acta Metall.* 1 (1953) 428.
- [7] G. Caginalp, W. Xie, *Phys. Rev. E* 48 (1993) 1897.
- [8] D.I. Popov, Ph.D. Thesis, Clarkson University. Video at <http://www.clarkson.edu/projects/eutectic/eutphfd.zip>.
- [9] V.M. Glazov, L.M. Pavlova, *Chemical Thermodynamics and Phase Equilibria*, 2nd edition, Moscow, Metall. 1988 (in Russian).